Journal of Ceramic Processing Research. Vol. 13, No. 5, pp. 579~585 (2012)

JOURNAL OF
Ceramic
Processing Research

Chemical expansion of water splitting oxygen separation membranes of $La_{0.7}Sr_{0.3}Cu_{0.2}Fe_{0.8}O_{3-\delta}$

H.-N. Im[a], S.-Y. Jeon[a], M.-B. Choi[a], J.-Y. Park[b] and S.-J. Song[a,]*

[a]*Department of Materials Science and Engineering, Chonnam National University, 300 Yongbong-dong, Buk-gu, Gwangju, 500-757, Korea*

[b]*Department of Advanced Materials Engineering, Sejong University, Seoul 143-747, Korea*

Mixed ionic-electronic conducting $La_{0.7}Sr_{0.3}Cu_{0.2}Fe_{0.8}O_{3-\delta}$ (LSCF7328) oxygen separation membranes are proposed for hydrogen production by water splitting because of their good electrocatalytic activity with a wide range of chemical stability. The properties of hydrogen production by water splitting and the isothermal expansion properties of LSCF7328 were measured as a function of temperature, CO content as a reducing agent, and water vapor pressure. The average expansion coefficient was about 13×10^{-6} K^{-1} below 973 K, corresponding to thermal expansion, and about 20×10^{-6} K^{-1} between 1073 K and 1273 K, corresponding to a combination of thermal and chemical expansion. Both the chemical diffusivity of oxygen and the surface exchange kinetics were successfully extracted from the transient chemical expansion relaxation profile using Fick's second law. The activation energy for oxygen ionic conductivity was calculated from the Nernst-Einstein equation as 1.31 eV.

Key words: Water splitting, Chemical expansion, Ionic conductivity.

Introduction

In recent years, hydrogen has received intensive attention both directly as a fuel and indirectly as an aide for fuel synthesis and semiconductor industries to meet demanding environmental regulations [1-3]. Among several different approaches followed for producing sufficient hydrogen, electrochemical hydrogen separation with hydrogen transporting membranes has been intensively investigated because of the high purity of the hydrogen separated from the feed stream with the non-requirement for an external power supply to drive the separation [4-7]. However, during extraction of hydrogen from hydrocarbon gases, the use of nonrenewable resources inevitably leads to the generation of carbon dioxide that necessitates a further sequestration process [8, 9]. To circumvent the carbon dioxide formation, hydrogen production from water has been considered as an alternative strategy. Hydrogen production by water splitting using oxygen separation membranes [10-12] has been recognized as a practical choice due to their unique ability to shift the water dissociation reaction equilibrium in hydrogen-enriched steam when oxygen is removed by mixed conducting oxygen separation membranes.

Because hydrogen production by water splitting is a direct result of oxygen permeation through membranes, the oxygen separation membranes should be investigated according to the factors affecting the hydrogen production rate [13, 14]: (i) ambipolar (oxygen ion and electron) conductivity, (ii) oxygen partial pressure (pO_2) gradient, (iii) temperature, (iv) membranes thickness, and (v) surface oxygen exchange kinetics. Recent research [15, 16] on hydrogen production by water splitting using oxygen separation membranes has mainly focused on proving the working principle of extensive hydrogen production by applying coal gas, i.e., a CO/CO_2 gas mixture, as a reactive gas on the oxygen permeated side of the membrane.

Non-reacting mixed conducting oxides with a CO/CO_2 mixture of $La_{0.7}Sr_{0.3}Cu_{0.2}Fe_{0.8}O_{3-\delta}$ (LSCF7328), a well-known mixed oxygen ionic-electronic conductor, have attracted considerable attention for use in a wide range of applications, such as cathodes for low- to intermediate-temperature solid oxide fuel cells [17-19] and dense oxygen separation membranes [20-21], because of their good electrocatalytic activity and chemical stability down to pO_2 of 10^{-15} atm at 1123 K. One of the major concerns for membrane application is the large oxygen deficiency of LSCF7328, which affects not only the oxygen transport property and redox stability, but also the thermal and chemical expansion ascribed to the difference in the lattice expansion applied across the membranes. The literature suggests that a LSCF7328 membrane readily undergoes oxygen deficiency, leading to an irreversible composition because Fe^{4+} cations are easily reduced to trivalent and further divalent cations with decreasing pO_2 following by the additional Cu^{3+} reduction to Cu^{2+} [22-24]. However, no major changes in crystal structure were

*Corresponding author:
Tel : +82-62-530-1706
Fax: +82-62-530-1699
E-mail: song@chonnam.ac.kr

revealed in X-ray diffraction (XRD) experiments, suggesting that lattice distortions were caused by the change in local coordination due to the preferential reduction of B-site cations with decreasing pO_2 [25].

In this study, LSCF7328 was applied to an oxygen separation membrane for hydrogen production by water splitting with a CO/CO_2 mixture reducing gas on the oxygen permeated side of the membrane. First, the hydrogen production rate was examined as a function of temperature, steam partial pressure and CO content. Then, the total expansion of LSCF7328 ascribed to the B-site cation reduction was investigated as a function of temperature and pO_2. Both the chemical diffusivity of oxygen and the surface exchange kinetics were uniquely estimated by the chemical expansion relaxation technique, and the ionic conductivity was calculated from the Nernst-Einstein equation connecting the oxygen self-diffusivity from chemical diffusivity using the thermodynamic enhancement factor.

Experimental

Perovskite LSCF7328 powders were prepared by a conventional solid state reaction method. The starting materials of $LaCO_3$ (Aldrich, 99.99%), $SrCO_3$ (Aldrich, 99.99%), F_2O_3 (Aldrich, 99.9%), and CuO (Aldrich, 99.9%) were weighed in the stoichiometric proportions of LSCF7328. The powders were mixed, ground in a ball mill with stabilized zirconia balls, and calcined at 1323 K for 10 h in air. The calcined oxide powders were then crushed, sieved to < 45 μm, pressed into pellets cold isostatically pressed at 150 MPa, and sintered at 1423 K for 10 h in air. As shown in Fig. 1, the XRD spectrum confirmed the attainment of a single phase, orthorhombic LSCF7328 via the solid state reaction method. A scanning electron microscopy (SEM; Shimadzu, SS-550) image of the as-sintered surface is shown in Fig. 2 and reveals well developed grains with a reasonable density at 95% of the theoretical value.

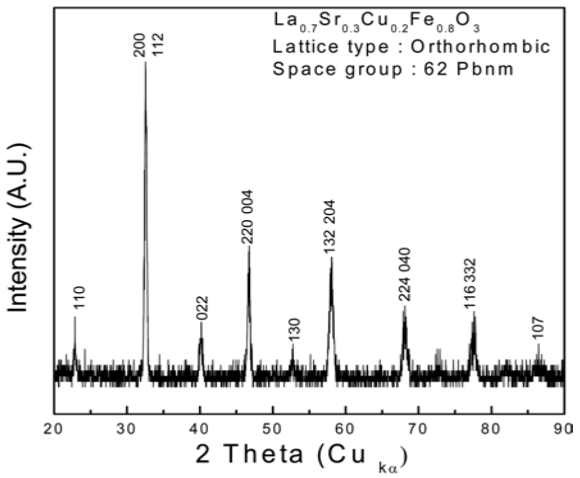

Fig. 1. Room-temperature X-ray diffraction (XRD) patterns of $La_{0.7}Sr_{0.3}Cu_{0.2}Fe_{0.8}O_{3-\delta}$ calcined at 1323 K for 10 h in air.

The hydrogen production rate by water splitting was measured on 0.36-mm-thick dense disks (≈ 94% theoretical, 12 mm in diameter). The planar surface of each disk was polished with 600-grit SiC paper and then affixed to an alumina tube. A seal was formed when the assembly was heated to 1173 K and spring-loaded rods squeezed a copper ring between the membrane and the alumina tube. To establish the oxygen potential gradients across the membranes, a "reducing" gas (a $CO\text{-}CO_2$ mixture) was flowed into the reducing side of the membrane. An oxidizing gas comprising nitrogen with 100 ppm hydrogen was bubbled through a water bath (EX-35D1 heating bath, Fisher Scientific). The hydrogen production rate at the oxidizing side was analyzed with an Agilent 6890 gas chromatograph. Leakage of gas through pores in the sample or through an incomplete seal was identified by measuring the He content of the permeate stream. Experimental data were only collected when the leakage rate was less than 1%. In order to minimize the edge contribution to the permeation, the membrane edge was sealed with a ceramic sealant. The feed and sweep gases were at ambient pressure. The experimental details are described elsewhere [26].

For isothermal dilatometry, parallelepiped specimens of dimensions $3.0 \times 3.0 \times 14.1\ mm^3$ were cut out of the sintered samples with a low-speed diamond saw. The one-dimensional displacement in the direction of the specimen length was measured using a Netzch L75 PT1600 dilatometer from room temperature to 1273 K at $2\ K\cdot min^{-1}$ with an air purge at a flow rate of $100\ cc\cdot min^{-1}$. The overall measurements were repeated over the temperature range of 298 K to 1273 K. For the chemical expansion relaxation measurements, each specimen was completely equilibrated in a given thermodynamic condition and then the oxygen chemical potential was abruptly changed to a different value while recording the specimen's total expansion vs. time until a new equilibrium was reached. The pO_2 values were controlled by flowing O_2/N_2 gas mixtures, and monitored with a zirconia-based oxygen sensor. The experimental details are described elsewhere [27].

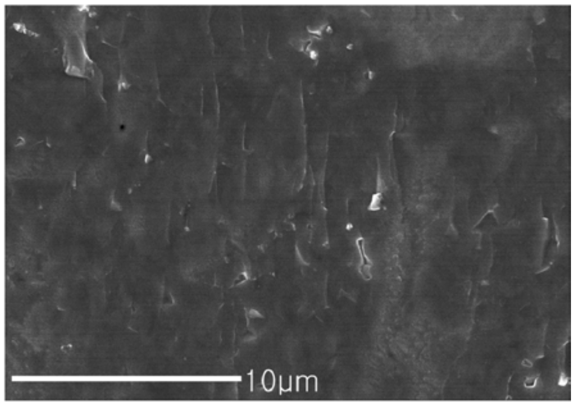

Fig. 2. Fracture surface scanning electron microscopy (SEM) micrographs of as-sintered $La_{0.7}Sr_{0.3}Cu_{0.2}Fe_{0.8}O_{3-\delta}$.

Results and Discussion

The hydrogen production rates were measured as a function of carbon monoxide content as a reducing gas at various water partial pressures at 1123 K for a 0.36-mm-thick LSCF7328 membrane, as shown in Fig. 3. The hydrogen production rate increased with increasing CO content because of the decreased pO_2, which increased the driving force for oxygen permeation from the oxidizing to the reducing side. After measurement at 80% CO/balance CO_2 gas mixture at 1173 K, the re-measured value of the hydrogen production rate at 10% CO/balance CO_2 gas mixture was identical within the experimental error at 1173 K, suggesting that LSCF7328 was chemically stable under the water splitting reaction with a CO-rich gas stream as a reducing agent.

Fig. 4 shows the water vapor pressure effect on the hydrogen production rate at 10% CO and 80% CO/balance CO_2, gas mixtures as a reducing gas at 1173 K. With increasing water vapor pressure in the oxidizing gas, more hydrogen was produced. Because the increased hydrogen production rate from the water splitting is a direct result of oxygen permeation from the oxidizing side, the results were attributed to an increased pO_2 gradient across the membrane for oxygen diffusion. The hydrogen production rate of 0.03 cm^3(STP)/min-cm^2, obtained at 1173 K with 80% CO/balance CO_2 at the oxygen permeated side and 0.03 atm of water vapor pressure at the oxidizing side, was subsequently increased to 0.12 $cm^3 \cdot min^{-1} \cdot cm^{-2}$ with a 0.36-mm-thick membrane at 1173 K when the water vapor pressure was increased to 0.49 atm at the oxidizing side of membrane. The experimental results clearly confirmed the potential application of the LSCF7328 membrane as a water splitting oxygen separation membrane using coal gas as a reducing gas without any loss in hydrogen production performance due to the good chemical resistance to carbon forming. However, the overall hydrogen production rate was an order of magnitude smaller than that of cermet membranes as oxygen separation membranes and the long-term stability has not been confirmed [11, 12, 26].

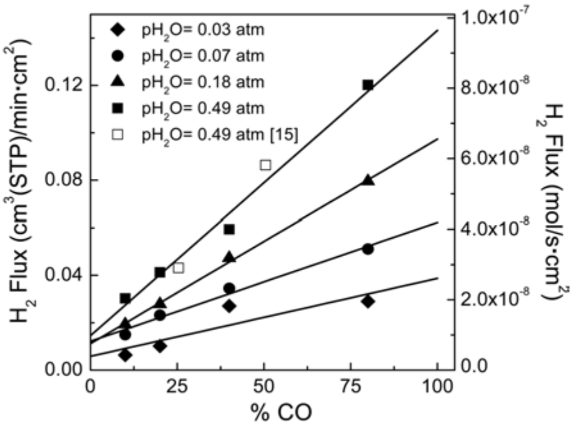

Fig. 3. Hydrogen production rate of ≈ 0.36-mm-thick $La_{0.7}Sr_{0.3}Cu_{0.2}Fe_{0.8}O_{3-\delta}$ vs. CO concentration in the gas mixture on the oxygen permeated side balance by CO_2 at various water vapor pressures.

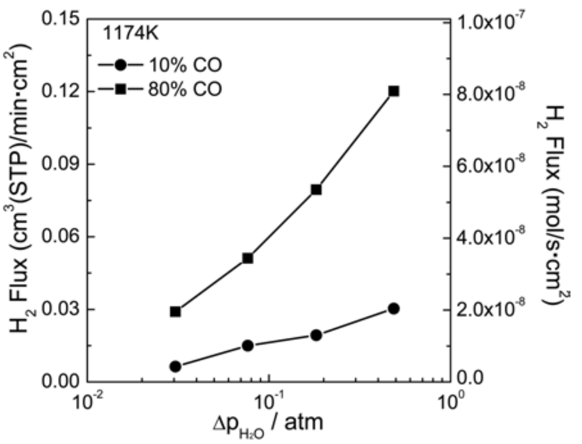

Fig. 4. Hydrogen production rate of ≈ 0.36-mm-thick $La_{0.7}Sr_{0.3}Cu_{0.2}Fe_{0.8}O_{3-\delta}$ vs. water vapor pressure on the hydrogen generating side balance by N_2 at various CO contents.

Fig. 5 shows the dependence of the hydrogen production rate on temperature with a CO contents ≈ 0.1, 0.2, 0.4, 0.8 atm in the oxygen permeated side and a water vapor pressure of 0.49 atm in the high steam

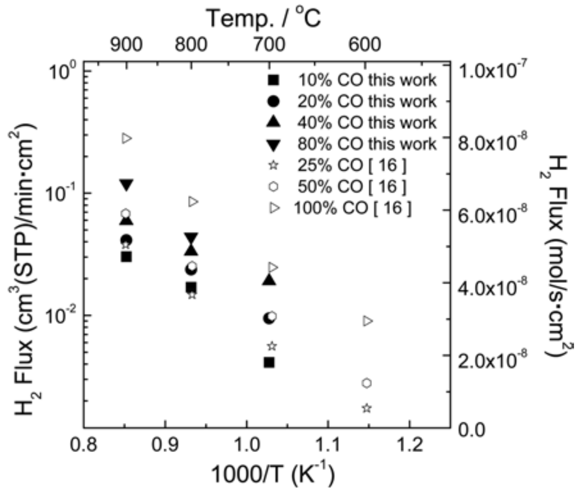

Fig. 5. Hydrogen production rate of ≈ 0.36-mm-thick $La_{0.7}Sr_{0.3}Cu_{0.2}Fe_{0.8}O_{3-\delta}$ vs. reciprocal temperature at various CO contents at the oxygen permeated side.

Table. 1. Activation energy values for the water splitting hydrogen production by $La_{0.7}Sr_{0.3}Cu_{0.2}Fe_{0.8}O_{3-\delta}$.

CO(g)/%	Activation energy/eV	Reference
10%	$(2.96 \pm 0.2) \times 10^{-2}$	this work
20%	$(3.59 \pm 0.4) \times 10^{-2}$	this work
25%	$(2.29 \pm 0.7) \times 10^{-2}$	[15]
40%	$(4.52 \pm 1.0) \times 10^{-2}$	this work
50%	$(4.11 \pm 1.4) \times 10^{-2}$	[15]
80%	1.9×10^{-1}	this work
100%	$(1.69 \pm 0.7) \times 10^{-1}$	[15]

oxidizing side. The CO contents and apparent activation energies are listed in the table 1. The activation energies differ for the different CO contents due to the effect of the difference in the resulting pO_2 at the reducing side of the membrane on the driving force for transporting oxygen. Note that the reference data [15] were normalized for the same thickness for the comparison.

The thermal expansion of LSCF7328 in the temperature range of 293 K to 1273 K in air is shown in Fig. 6(a). The expansion curve was completely reversible during heating/cooling cycling in air. The total lattice expansion induced during high temperature redox cycles can be expressed by the thermal expansivity (β_T) and the chemical expansivity (β_c):

$$\beta_T=\left(\frac{\partial ln\hat{V}}{\partial T}\right)_{X_V,P} \quad \beta_C=\left(\frac{\partial ln\hat{V}}{\partial X_V}\right)_{T,P} \tag{1}$$

where $\hat{V}$ is the specific volume, T the temperature, P the total pressure, and x_v the oxygen vacancy mole fraction, defined as $x_v = \delta/3$, where δ is the oxygen nonstoichiometry. Thus, β_T and β_c may be separated, as shown in Fig. 6(a), as indicated by the dashed lines. In this figure, the chemical expansion became noticeable above 973 K, which was attributed to the thermally-induced loss of lattice oxygen and the formation of oxygen vacancies associated with the change in the B-site cation (Cu and Fe) oxidation state. The oxygen stoichiometry calculated from the thermogravimetric analysis indicated that the oxygen vacancy content in the formula unit is around 0.25 near 1123 K at pO_2 of 10^{-12} atm [25]. From the isothermal oxygen nonstoichiometry data, the predominant B-site cations were identified as Fe^{3+} in the oxidizing atmosphere and Fe^{2+} as pO_2 was decreased followed by the Cu reduction to Cu^{2+} in LSCF7328. Although each cation's contribution to the chemical expansion could not be differentiated, both cation reductions were accompanied by lattice oxygen release from the external reaction with temperature due to the linear increase of the chemical expansion at high temperature, according to the following reaction:

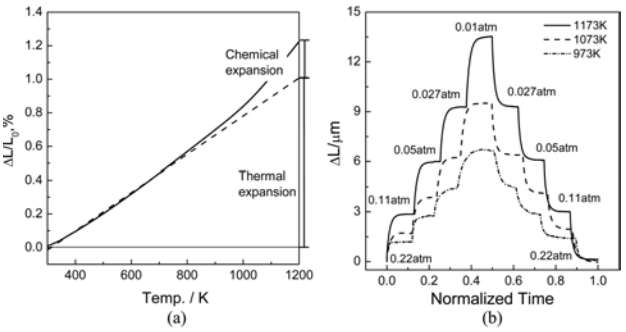

Fig. 6. Total expansion curve for $La_{0.7}Sr_{0.3}Cu_{0.2}Fe_{0.8}O_{3-\delta}$ (a) in the temperature range of 293 K ~ 1273 K at air, and (b) in the oxygen partial pressure (pO_2) range of 0.01 to 0.21 atm at various temperatures.

$$\frac{1}{2}O_2(g)+V_O^{\bullet\bullet}+2M_M^{/}=O_O^x+2M_M^x \tag{2}$$

The average expansion coefficient was about 13×10^{-6} K^{-1} below 973 K, corresponding to thermal expansion, and about $20 \times 10^{-6} K^{-1}$ between 1073 K and 1273 K, corresponding to a combination of thermal and chemical expansion.

Furthermore, a raw trace of the relative isothermal dilatometry measurements at various temperatures is shown in Fig. 6(b) as pO_2 was step increased from 0.01 atm to air pressure. The change in pO_2 was set sufficiently small ($\Delta logP_{O_2} < 1$) so that the chemical diffusivity might be regarded as constant within the experimental window. The good reversibility of the chemical expansion of LSCF7328 within the experimental conditions suggests that the external redox reaction reflects the change in the nonstoichiometry of LSCF7328. The chemical expansion increased linearly with both increasing temperature and decreasing pO_2, which was ascribed to the repulsion within the unit cell because the effective negative charge of the reduced B-site cation in the lattice induced electrostatic charges that repelled their nearest oxygen atoms. As the temperature was increased, the induced chemical expansion of LSCF7328 became dominant. This expansion may be the limiting factor in the oxygen separation application of the LSCF7328 membrane when applied as 10 ~ 100-μm-thick sections in real operating membranes because the chemical strain, which arises from the differential chemical expansion at both sides of the oxygen separation membrane operating under a considerable pO_2 gradient at elevated temperature, may induce microcracks to propagate into the membrane fracture.

The chemical expansion relaxation response with a pO_2 change could be considered as a direct function of the oxygen vacancy concentration, in which case the

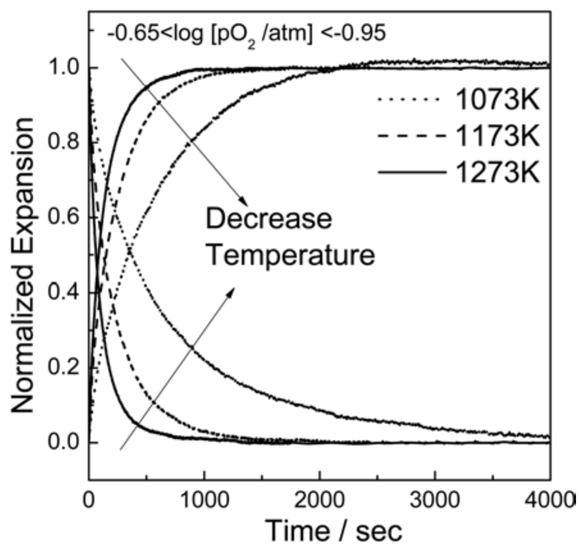

Fig. 7. Normalized raw trace of the isothermal expansion of $La_{0.7}Sr_{0.3}Cu_{0.2}Fe_{0.8}O_{3-\delta}$ for logarithmic oxygen partial pressures (pO_2) of -0.65 to -0.95 atm at various temperatures.

kinetic parameters could be extracted from the transient dilatometry measurements because the gas switch-out time was sufficiently brief to enable a reliable fit of the oxidation and reduction kinetics. The normalized relaxation profiles of the mean total expansion are shown as a function of temperature at an identical oxygen activity window in Fig. 7 at a fixed pO_2 window. During the redox reaction, the oxygen is either incorporated into or released from the LSCF7328 membrane. For a small displacement from equilibrium, the transient behavior in the equilibrium process can be best fitted with Fick's second law, and a more detailed derivation of this equation may be found in references [28-30]:

$$\frac{\varepsilon(t)-\varepsilon_0}{\varepsilon_\infty-\varepsilon_0}=1-\left[\sum_{n=1}^{\infty}\frac{2(\beta_n tan\beta_n)^2 exp\left(-\frac{\beta_n^2 D_{chem.}(t-t_0)}{a^2}\right)}{\beta_n^2(\beta_n^2+(\beta_n tan\beta_n)^2+\beta_n tan\beta_n)}\right]^2 \quad (3)$$

where β_n is the positive root of

$$L=\beta_n tan\beta_n = ak_{chem}/D_{chem} \quad (3\text{-a})$$

where ε_0 and ε_∞ denote the equilibrium total expansivity before (t = 0) and after (t = ∞) the relaxation, respectively, L is the diffusion length, i.e., half a thickness of the bar-shaped specimen, t the time, κ the surface reaction rate constant, and $\tilde{D}$ the chemical-diffusion coefficient. The nonlinear least square fitting to the experimental relaxation shown in Fig. 7 reveals very good agreement with the transition expansion data, and thereby enabled the chemical diffusion coefficient to be determined. The results clearly show that the chemical diffusivity and surface exchange rate of oxygen increased within the investigated temperature range, as shown in Fig. 8.

Fig. 8 shows the temperature dependence of the chemical diffusion and surface reaction coefficient of LSCF7328, obtained from the oxidation chemical expansion relaxation in the temperature range of 973 K to 1273. The uncertainty level is within the symbol size of the data. k_{chem} is approximately two orders of magnitude larger that D_{chem} and the activation energy for D_{chem} is slightly larger than that of k_{chem}. The calculated D_{chem} value is larger than that of other fast ion-conducting perovskite oxides but k_{chem} is somewhat smaller.

The self-diffusion coefficient of oxygen, D_0, can also be calculated from the chemical diffusion coefficient for the LSCF7328 specimen using the relation of $D_{chem} = D_0\gamma_0$, where γ_0 is the thermodynamic enhancement factor given by [31]:

$$\gamma_0=\frac{1}{2}\left(\frac{\partial lnP_{O_2}}{\partial ln(3-\delta)}\right)_T \quad (4)$$

from the pO_2 dependence of the oxygen nonstoichiometry under isothermal conditions. Fig. 9 shows the temperature dependence of the self-diffusion coefficient of oxygen for the LSCF7328 specimen as estimated from the combination of the chemical diffusion coefficient and the thermodynamic enhancement factor calculated from isothermal nonstoichiometry in the literature [25]. The plot exhibits an Arrhenius-type behavior due to the nature of the thermally-activated diffusion process. From the temperature dependence of diffusivity in the air condition, the activation energy was calculated to be approximately 1.35 ± 0.12 eV:

$$D_0=(5.37\pm1.57)\times10^{-2}exp\left(-\frac{1.35\pm0.12eV}{kT}\right) \quad (5)$$

The ionic conductivity can be calculated using the Nernst-Einstein relation:

$$\sigma_{ion}=\frac{4F^2[V_0^{\bullet\bullet}]D_V}{RTV_m} \quad (6)$$

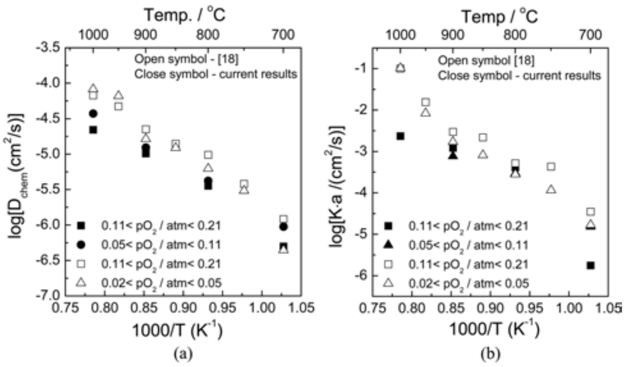

Fig. 8. (a) The chemical diffusion coefficient, and (b) the surface exchange coefficient of $La_{0.7}Sr_{0.3}Cu_{0.2}Fe_{0.8}O_{3-\delta}$ as a function of temperature.

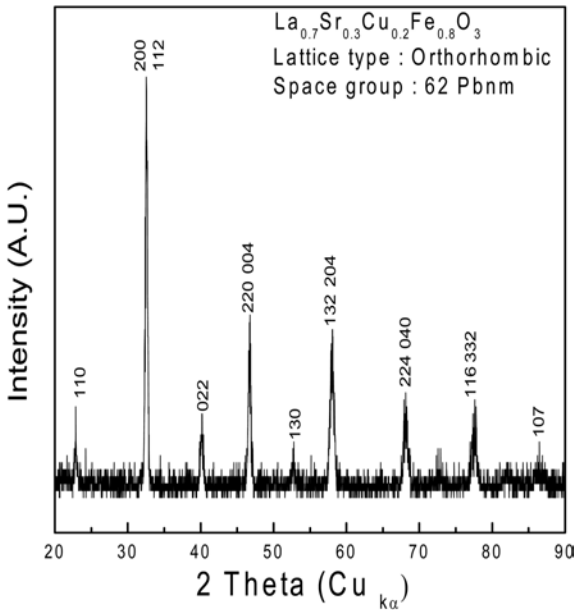

Fig. 9. Arrhenius plots of the oxygen self-diffusion coefficients and tracer diffusion coefficient for $La_{0.7}Sr_{0.3}Cu_{0.2}Fe_{0.8}O_{3-\delta}$ (the thermodynamic enhancement factor was calculated from isothermal nonstoichiometry data [25])

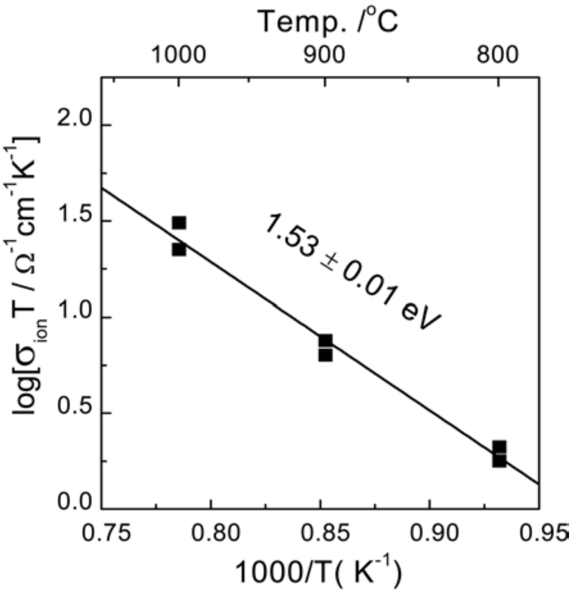

Fig. 10. Temperature dependence of the oxygen ionic conductivity of $La_{0.7}Sr_{0.3}Cu_{0.2}Fe_{0.8}O_{3-\delta}$ as calculated from the Nernst-Einstein relationship.

where V_m is the molar volume of the LSCF7328 specimen (= 54.873 $cm^3 \cdot mol^{-1}$), D_v the diffusion coefficient of oxygen vacancies, and $[V_O^{\bullet\bullet}]$ the oxygen vacancy concentration under the given thermodynamic conditions. Because the diffusion flux of oxide ions must be balanced by the diffusion flux of oxygen vacancy due to the structure constraint, the following relationship should be maintained:

$$[O_0^X]D_0 = [V_0^{\bullet\bullet}]D_V \tag{7}$$

The calculated self-diffusion coefficient of oxygen in Fig. 9 was combined with the equilibrium oxygen non-stoichiometry of the LSCF7328 specimen [25] to assess the partial oxygen ion conductivity by the Nernst-equation, as given in Eq. 7. Fig. 10 shows the calculated ionic conductivity as a function of temperature above 973 K. The plot reveals an ionic conductivity activation energy of 1.39 ± 0.14 eV in the air condition, best fitted by the following equation:

$$\sigma_{ion}T = 8.22\times10^{-1}exp\left(-\frac{1.53\pm0.01eV}{kT}\right) \tag{8}$$

Conclusions

The properties of hydrogen production by water splitting and the isothermal expansion properties of LSCF7328 were measured as a function of temperature, CO content as a reducing agent, and water vapor pressure. The logarithmic temperature dependence of the hydrogen production rates on the water vapor pressure in the oxidizing gas and on the carbon dioxide partial pressure (pCO) in the reducing gas was in agreement with the literature data from oxygen permeation measurements. The average expansion coefficient was about 13×10^{-6} K^{-1} below 973 K, corresponding to thermal expansion, and about 20×10^{-6} K^{-1} between 1073 K and 1273 K, corresponding to a combination of thermal and chemical expansion. The transient chemical expansion relaxation profile was best fitted with Fick's second law, for a small displacement from the equilibrium, and both the chemical diffusivity of oxygen and the surface exchange kinetics were successfully extracted. The oxygen ionic conductivity was calculated from the Nernst-Einstein equation by combining the oxygen self-diffusivity from the chemical diffusivity and the thermodynamic enhancement factor from the oxygen nonstoichiometry data in the literature.

Acknowledgement

This research was supported by the Fusion Research Program for Green Technologies through the National Research Foundation of Korea (NRF) funded by the Ministry of Education, Science and Technology (2011-0019303)

References

1. B. Sakintuna, F. Lamari-Darkrim, M. Hirscher, J. Hydrogen Energy, 32, 1121 (2007).
2. M. Ni, D.Y.C. Leung, and M.K.H. Leung, International Journal of Hydrogen Energy, 32, 3238 (2007).
3. R.W. Baker, Ind. Eng. Chem. Res., 41, 1393 (2002).
4. S.-J. Song, E.D. Wachsman, J. Rhodes, S.E. Dorris, and U. Balachandran, Solid State Ionics, 167, 99 (2004).
5. S.-J. Song, J.-H. Moon, T.-H. Lee, S. E. Dorris, and U. Balachandran, Solid State Ionics, 179, 1854 (2008).
6. S.-Y. Jeon, M.-B. Choi, C.-N. Park, E.D. Wachsman, and S.-J. Song, Journal of Membrane Science, 382, 323 (2011).
7. J.W. Phair, and S.P.S. Badwal, Science and Technology of Advance Materials, 7, 792 (2006).
8. N.Z. Muradov, International Journal of Hydrogen Energy, 18, 211 (1993).
9. C. Song, Catalysis Today, 77, 17 (1993).
10. H. Naito, H. Arashi, Solid State Ionics, 79, 366 (1995).
11. U. Balachandran, T.H Lee, S. Wang, and S.E. Dorris, United States Patent # 6468499, filing date 06/09/2000.
12. U. Balachandran, T.H Lee, S. Wang, and S.E. Dorris, International Journal of Hydrogen Energy, 29, 291 (2004).
13. U. Balachandran, T.H Lee, and S.E. Dorris, International Journal of Hydrogen Energy, 32, 451 (2007).
14. V.V. Kharton, A.A. Yaremchenko, A.V. Kovalevsky, A.P. Viskup, E.N. Naumovich, and P.F. Kerko, Journal of Membranes Science, 163, 307 (1999).
15. P.N. Dyer, R.E. Richards, S.L. Russek, and D.M. Taylor, Solid State Ionics, 134, 21 (2000).
16. C.-Y. Park, T.-H. Lee, S.E. Dorris, Y. Lu, and U. Balachandran, International Journal of Hydrogen Energy, 36, 9345 (2011).
17. C.-Y. Park, T.-H. Lee, S.E. Dorris, and U. Balachandran, International Journal of Hydrogen Energy, 35, 4103 (2010).
18. J. Wackerl, T. Koppitz, D.-H. Peck, S.-K. Woo, and T. Markus, J. Appl. Electrochem., 39, 1243 (2009).

19. G. Coffey, J. Hardy, O. Marina, L. Pederson, P. Rieke, and E. Thomsen, Solid State Ionics, 175, 73 (2004).
20. O.A. Marina, L.R. Pederson, M.C. Williams, G.W. Coffey, K.D. Meinhardt, C.D. Nguyen, and E.C. Thomsen, J. Electrochem. Soc., 154, B452 (2007).
21. M. Sogaard, P.V. Hendriksen, and M. Mogensen, J. Solid State Chemistry, 180, 1489 (2007).
22. L. Nalbandian, A. Evodu, and V. Zaspalis, Int. J. Hydrogen Energy, 36, 6657 (2011).
23. I. Kaus, H.U. Anderson, Solid State Ionics, 129, 189 (2000).
24. G.W. Coffey, J. Hardy, L.R. Pedersen, P.C. Rieke, E.C. Thomsen, and M. Walpole, Solid State Ionics, 158, 1 (2003).
25. X. Ding, C. Cui, X. Du, and L. Guo, J. Alloys and Compounds, 475, 418 (2009).
26. C.-Y. Park, F.V. Azzarello, and A.J. Jacobson, J. Materials Chemistry, 16, 3624 (2006).
27. S.-J. Song, J.-H. Moon, H.-W. Ryu, T.-H. Lee, S. E. Dorris, & U. Balachandran, Journal of Ceramic Processing Research, 9, 123 (2008).
28. M.-B. Choi, S.-Y. Jeon, H.-S. Yang, J.-Y. Park, and S.-J. Song, Journal of the Electrochemical Society, 158, B189 (2011).
29. S.B. Adler, J. Amer. Ceram. Soc., 84, 2117 (2001).
30. S.P. Timoshenko, J.N. Goodier, Theory of Elasticity. 3rd Ed., McGraw Hill, New York (1969).
31. X. Chen, J. Yu, and S.B. Adler, Chem. Mater., 17, 4537 (2005).
32. P.J. Gelling, H.J. M. Bouwmeester (Eds), The CRC Handbook of Solid State Electrochemistry, Chap. 14, CRC Press, New York (1997).